Far-infrared photodetection in graphene nanoribbon heterostructures with black-phosphorus base layers

**Maxim Ryzhii,[a,]* Victor Ryzhii,[b,c,d,e] Petr P. Maltsev,[c]
Dmitry S. Ponomarev,[c,d] Vladimir G. Leiman,[d] Valery E. Karasik,[e]
Vladimir Mitin,[f] Michael S. Shur,[g,h] and Taiichi Otsuji[b]**

[a]University of Aizu, Department of Computer Science and Engineering, Aizu-Wakamatsu, Japan

[b]Tohoku University, Research Institute of Electrical Communication, Sendai, Japan

[c]Institute of Ultra-High Frequency Electronics of RAS, Moscow, Russia

[d]Moscow Institute of Physics and Technology, Center of Photonics and Two-Dimensional Materials, Dolgoprudny, Russia

[e]Bauman Moscow State Technical University, Center of Photonics and Infrared Engineering, Moscow, Russia

[f]University at Buffalo, SUNY, Department of Electrical Engineering, Buffalo, New York, United States

[g]Rensselaer Polytechnic Institute, Department of Electrical, Computer, and Systems Engineering, Troy, New York, United States

[h]Electronics of the Future, Inc., Vienna, Virginia, United States

Abstract. We propose far-infrared photodetectors with the graphene nanoribbon (GNR) array as the photosensitive element and the black phosphorus (bP) base layer (BL). The operation of these GNR infrared photodetectors (GNR-IPs) is associated with the interband photogeneration of the electron–hole pairs in the GNR array followed by the tunneling injection of either electrons or holes into a wide gap bP BL. The GNR-IP operating principle is akin to that of the unitraveling-carrier photodiodes based on the standard semiconductors. Due to a narrow energy gap in the GNRs, the proposed GNR-IPs can operate in the far-, mid-, and near-infrared spectral ranges. The cut-off photon energy, which is specified by the GNR energy gap (i.e., is dictated by the GNR width), can be in the far-infrared range, being smaller that the energy gap of the bP BL of $\Delta_G \simeq 300$ meV. Using the developed device models of the GNR-IPs and the GNR-IP terahertz photomixers, we evaluate their characteristics and predict their potential performance. The speed of the GNR-IP response is determined by rather short times: the photocarrier try-to-escape time and the photocarrier transit time across the BL. Therefore, the GNR-IPs could operate as terahertz photomixers. The excitation of the plasma oscillations in the GNR array might result in a strong resonant photomixing. © *The Authors. Published by SPIE under a Creative Commons Attribution 4.0 Unported License. Distribution or reproduction of this work in whole or in part requires full attribution of the original publication, including its DOI.* [DOI: 10.1117/1.OE.60.8.082002]

1 Introduction

The quantization of the energy spectrum in the graphene nanoribbon (GNR) arrays, obtained by partitioning of the graphene layer (GL), results in the transformation of the two-dimensional gapless spectrum of the electrons and holes to the spectrum consisting of the sets of one-dimensional subbands. Such a quantization also leads to the formation of the energy gap in the GNRs.[1–8] The transformation of the energy spectrum brings about substantial modifications of the radiation absorption characteristics of the GNRs compared with the uniform GLs.

---

*Address all correspondence to Maxim Ryzhii, E-mail: m-ryzhii@u-aizu.ac.jp

These modifications include the appearance of the absorption resonances associated with the radiative transitions between the hole sub-bands tops and the electron sub-bands bottoms and the appearance of the absorption "red" edge.[6,8] These features of the GNR radiation absorption can be used in different infrared optoelectronic devices. The incorporation of the black-phosphorus (bP) layers, exhibiting the interband absorption of the photons with the energies from $\hbar\Omega \simeq 300$ to 2000 meV depending on the bP layer thickness, opens new prospects.[9–19] The heterostructures, in which GLs or GNR arrays are integrated with the bP layers, can exhibit additional functionalities.[20–26] This is due to the special GL and GNR and the bP layers' band alignment (the Dirac point in the GLs and GNRs corresponds to the energy gap in the bP) and relatively narrow energy gap ($\Delta_G \simeq 300$ meV) in the bP layers with a sufficiently large number of atomic sheets.[27] The GL- and GNR-heterostructures with the black-arsenic (bAs) layers having even smaller band gaps[28–32] demonstrate similar properties.

The GNR infrared photodetectors have been (GNR-IPs) proposed and analyzed previously[6,8,33] using the interband transitions. In those IPs, the carrier photogeneration leads to an increase in the GNR longitudinal conductivity. In contrast, here, we consider the GNR-based vertical IPs using the radiation interband absorption in the GNR arrays. We focus our analysis on the GNR-IPs with the undoped (weakly doped) GNR array sandwiched between the top cap layer (CL) doped by donors (with the donor surface density Σ_d) and the bP base layer (BL) doped by acceptors (with the surface density Σ_a). The BL is lying on the contact layer (substrate) of p^+-type (see Fig. 1). The CL can be either the n-bP BL or made of other materials, in particular, hexagonal boron nitride (hBN). An example is the GNR-IP based on n-bP/GNR/p-bP/p^+-bP heterostructure or on an n-hBN/GNR/p-bP/p^+-bP heterostructure. The GNR array is supplied by the side n-type contact to each GNR, so that the GNR array with the contact forms a fork-like structure as shown in Fig. 1. The donors in the CL and acceptors in the BL can be spatially distributed uniformly across these layers or be concentrated in the delta-doped sheets. The GNR array plays the role of the photoemitter replacing the GL-photoemitter.[26] The GNR-IP operation is associated with the emission of the photoexcited holes from the GNR due to tunneling into p-BL contributing to the terminal current.

For the detection of radiation with $\hbar\Omega > 300$ meV, one can use more or less standard photodiodes using the interband transitions in bulk bP layers.[16] We limit our consideration to the photon energies $\hbar\Omega < \Delta_G$, where $\Delta_G \simeq 300$ meV is the energy gap in the bP BL. The band diagram of the GNR-IP with n-CL and p-BL is shown in Fig. 2. Such a choice of the device structure is associated with a relative smallness of the valence band off-set Δ_V at the GNR/bP interface in comparison with the pertinent conduction band off-set Δ_C. This implies that the IPs of the n-bP/GNR/p-bP/p^+-bP type can have smaller cut-off photon energy (in the far-infrared or even in the terahertz ranges) compared to the IPs of the p-bP/GNR/n-bP/n^+-bP type. The GNR-IPs based on heterostructures of the latter type can be considered analogously.

At $\Sigma = \Sigma_d - \Sigma_a + \kappa_{BL}V/4\pi eW > 0$, where κ_{BL} and W are the BL dielectric constant and thickness, respectively, and V is the bias voltage, the Fermi level in the GNRs is in the conduction band, i.e., $\varepsilon_{GNR}^F > 0$ [see Fig. 2(a)].

The operation principle of the GNR-IPs resembles that of the unitraveling-carrier photodiodes[34–36] with a bulk absorbing layer serving as the emitter with the diffusive supply of the carriers injected into the BL.

Since the electric field in the p-BL is high, all the holes injected from the GNR can reach the p^+ substrate. As a result, the current is determined solely by the injection from the GNR
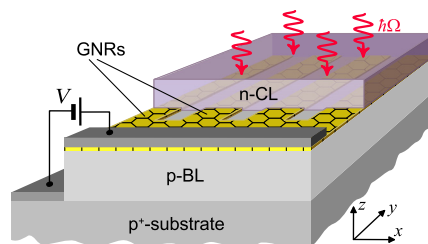
Fig. 1 Schematic view of the GNR-IP device structure.
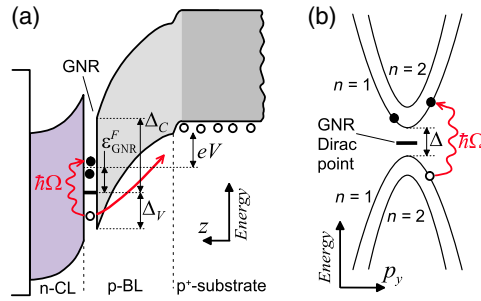
Fig. 2 (a) The GNR-IP band diagram with tunneling of the photoexcited holes under bias voltage and (b) interband electron transitions between the sub-bands ($n = 1 \rightarrow n = 1$ and $\Delta < \hbar\Omega < 2\Delta$) in the GNR valence and conduction bands. The open and opaque circles correspond to the holes and electrons, respectively.

[as schematically shown in Fig. 1(a)], so that the specific of the hole transport in the p-BL (ballistic or drift) does not affect the steady-state characteristics. However, the hole transit time across the p-BL can be fairly different in the cases of ballistic and drift transport (see Sec. 4). In this regard, the situation is analogous to that in the unitraveling-carrier photodiodes.

2 Main Equations

The electron and hole, $\varepsilon^-(p)$ and $\varepsilon^+(p)$, energy spectra in GNRs can be presented as the sets of the one-dimensional sub-bands[6–8] [see Fig. 2(b)]

$$\varepsilon^{\mp} = \pm v_W \sqrt{p^2 + (\pi\hbar/d)^2 n^2}, \tag{1}$$

where $p = p_y$ is the carrier momentum along the GNR (in the y direction), $v_W \simeq 10^8$ cm/s is the characteristic carrier velocity in GLs (and GNRs), and $n = 1, 2, 3, \ldots$ is the index of the sub-band in the valence band (lower sign) and the conduction band (upper sign). The energy spectrum given by Eq. (1) corresponds to the GNR energy gap $\Delta = 2\pi v_W \hbar/d$ and the carrier effective mass (near the sub-band's top and bottom) $m = \Delta/2v_W^2$. At $d = 15$ to 90 nm, in agreement with the experimental data,[3] one obtains $\Delta \simeq (300 - 30)$ meV and $m \simeq (0.01 - 0.002)m_0$,[7] where m_0 is the electron mass in vacuum.

Under the steady-state irradiation by the photon flux I_Ω with the photon energy $\hbar\Omega$, the average photocurrent density $\langle j_\Omega \rangle$ and the GNR-IP responsivity $R_\Omega = \langle j_\Omega \rangle / \hbar\Omega I_\Omega$ are given by (see also the Appendix)

$$\langle j_\Omega \rangle = e\beta_\Omega \Theta_\Omega I_\Omega. \tag{2}$$

Here, e is the electron charge, β_Ω is the ratio of the flux of the incident photons absorbed in the GNR array due to the interband transitions to the flux of the incident photons I_Ω (the average photon interband absorption coefficient of the GNR), and Θ_Ω is the probability of the photo-excited holes escape from the GNR. As seen from Eq. (2), the photocurrent in the GNR-IPs with the vertical injection is determined not only by the absorption coefficient, but also by the escape probability of the photoexcited carriers (holes) Θ_Ω (as in the interband GL-IDs,[26] see also references therein). For the normal radiation incidence, the GNR array interband absorption coefficient is given by[6,8]

$$\beta_\Omega = \beta \left(\frac{2d}{\pi D}\right) \left(\frac{\Delta}{\hbar\Omega}\right) S_\Omega \sum_{n=1}^{\infty} \mathcal{F}_n \left(\frac{\hbar\Omega}{\Delta}\right). \tag{3}$$

Here, $\beta = \pi e^2 / c\hbar\sqrt{\kappa} \simeq \pi/137\sqrt{\kappa}$, c is the speed of light, κ is the refractive index determined by the dielectric constants of the CL and BL, κ_{CL} and κ_{BL}, respectively, and the factor d/D is the fraction of the GNR-IP area covered by the GNR array (the GNR aspect ratio). The function

$$S_{\Omega} = \frac{\exp\left(\frac{\hbar\Omega}{2T}\right)}{2\left[\cosh\left(\frac{\hbar\Omega}{2T}\right) + \cosh\left(\frac{\varepsilon_{\text{GNR}}^F}{T}\right)\right]} \tag{4}$$

accounts for the Pauli principle for the interband transitions in the GNR (with the Fermi energy $\varepsilon_{\text{GNR}}^F$ counted from the Dirac point at the temperature T), whereas the function

$$\mathcal{F}_n(X) = \frac{1}{\sqrt{2\pi}\gamma} \int_n^{\infty} \frac{d\xi\,\xi}{\sqrt{\xi^2 - n^2}} \exp\left[-\frac{(\xi - X)^2}{2\gamma^2}\right] \tag{5}$$

describes the probability of the interband transitions in the GNR with the electron and holes states given by Eq. (1) and the Gaussian broadening (or smearing) of these states due the collisions, characterized by $\gamma = \Gamma/\Delta$, where $\Gamma \sim \hbar/\tau$ with τ being the electron and hole momentum relaxation time.

The quantity Θ_{Ω} in Eq. (2) is the tunneling escape probability of the photoexcited holes having the energy $\varepsilon_{\Omega} = (\hbar\Omega - \Delta)/2$ to escape from the GNR.

We estimate Θ_{Ω} as

$$\Theta_{\Omega} \simeq \frac{1}{1 + \frac{\tau_{\text{esc}}}{\tau_{\text{relax}}} \exp\left(\eta_{\Omega}^{3/2} \frac{E_{\text{tunn}}}{E_{\text{GNR}}}\right)}. \tag{6}$$

Here, $\eta_{\Omega} = 1 - \hbar\Omega/2\Delta_V$, $E_{\text{tunn}} = 4\sqrt{2m_z}\Delta_V^{3/2}/3e\hbar$ is the characteristic tunneling field, m_z is the hole effective mass in the BL in the direction perpendicular to the atomic sheets, τ_{relax} is the relaxation time of the photoexcited holes in the GNR due to the recombination and the energy relaxation on acoustic phonons, and τ_{esc} is the photoexcited holes' try-to-escape time. The electric field at the GNR array plane E_{GNR} determining the shape of the tunneling barriers depends on the potential drop V between the collector and the GNR. Considering the BL doping and neglecting the quantum capacitance,[37] we arrive at the following equation:

$$E_{\text{GNR}} \simeq \frac{V}{W} + E_a - E_d. \tag{7}$$

Here, $E_a = 4\pi e\Sigma_a/\kappa_{\text{BL}}$ and $E_d = 4\pi e\Sigma_d/\kappa_{\text{CL}}$.

Setting $\Delta_V = 100$ meV and $m_z \simeq 0.28m_0$,[10] we obtain $E_{\text{tunn}} \simeq 1.19 \times 10^6$ V/cm. For $\Sigma_a = 2.2 \times 10^{12}$ cm^{-2} and $\kappa_{\text{BL}} = 4$, we obtain $E_a \simeq 1 \times 10^6$ V/cm.

3 Spectral Characteristics of the GNR-IP Responsivity and Detectivity

According to Eq. (2), the GNR-IP responsivity R_{Ω}—one of the main IP characteristics—can be presented as

$$R_{\Omega} = \frac{2e\beta S_{\Omega}\Theta_{\Omega}}{\pi\hbar\Omega}\left(\frac{d}{D}\right) = \overline{R}_{\Omega}\frac{2}{\pi}\left(\frac{\Delta}{\hbar\Omega}\right)\sum_{n=1}^{\infty}\mathcal{F}_n\left(\frac{\hbar\Omega}{\Delta}\right). \tag{8}$$

Here,

$$\overline{R}_{\Omega} = \frac{e\beta S_{\Omega}\Theta_{\Omega}}{\hbar\Omega}\left(\frac{d}{D}\right). \tag{9}$$

Figure 3 shows the spectral characteristics of the GNR-IP responsivity calculated for parameters of the GNR-IP structure (Δ, Γ, $\varepsilon_{\text{GNR}}^F$, and T). The following parameters are assumed: $\beta = 1.15 \times 10^{-2}$, ($\kappa = 4$), $\Delta_V = 100$ meV, $\tau_{\text{esc}}/\tau_{\text{relax}} \simeq 0.1$, $E_{\text{tunn}} \simeq 1.19 \times 10^6$ V/cm ($m_z \simeq 2.5 \times 10^{-28}$ g), and $E_{\text{GNR}} = 1 \simeq 10^2$ V/μm. The temperature is assumed to be $T = 26$ meV ($T \simeq 300$ K) except for Fig. 3(d). The parameter Γ was assumed to be $\Gamma = 1$ and 5 meV, which corresponds to the realistic momentum relaxation times $\tau \simeq 6.25 \times 10^{-13}$ s and 1.25×10^{-13} s,
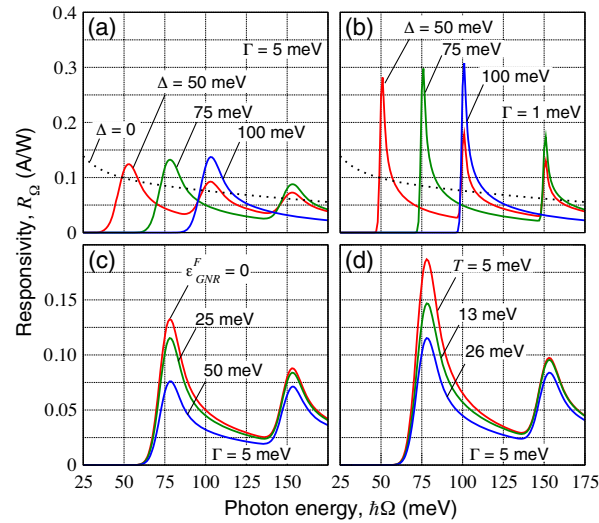
Fig. 3 The responsivity R_Ω versus photon energy $\hbar\Omega$ of GNR-IPs with (a) $\Gamma = 5$ meV and (b) $\Gamma = 1$ meV at different energy gaps Δ (different GNR widths), (c) $\Delta = 75$ meV, $\Gamma = 5$ meV, and $\varepsilon_{GNR}^F = 25$ meV at different Fermi energies in the GNR ε_{GNR}^F, and (d) $\Delta = 75$ meV, $\Gamma = 5$ meV, and $\varepsilon_{GNR}^F = 25$ meV at different temperatures T. Dotted lines correspond to the GL-IP responsivity.

respectively. At $\Delta = 100$ meV, the range of the Fermi energies $\varepsilon_{GNR}^F = 25$ to 50 meV corresponds to the $\Sigma_d - \Sigma_a \simeq (1.8 \text{ to } 4.4) \times 10^{12}$ cm^{-2}. For the degenerate electron gas in the GNRs (sufficiently large Σ), the Fermi energy in the GNRs $\varepsilon_{GNR}^F \simeq \Delta(\Sigma d^2/2)^2 \propto \Sigma/\Delta$ (see the Appendix).

At $\Delta = 75$ meV, the range of the Fermi energies $\varepsilon_{GNR}^F = 25$ to 50 meV corresponds to $\Sigma_d - \Sigma_a \simeq (2.4 \text{ to } 5.9) \times 10^{12}$ cm^{-2}.

As seen from the comparison of the dependences for GNR-IPs with those for the GL-IP (without the partitioning of the GL into the GNRs, i.e., with $\Delta = 0$, and presented by the dotted lines) shown in Figs. 3(a) and 3(b), the former can exhibit much higher R_Ω when $\hbar\Omega \sim \Delta$.

As follows from Figs. 3(c) and 3(d), an increase in the Fermi energy ε_{GNR}^F and in temperature T leads to a smaller responsivity. This is attributed to stronger restrictions for the radiative interband transitions imposed by the Fermi principle [described by the factor S_Ω given by Eq. (4)].

The GNR-IP detectivity is given by

$$D_\Omega^* = \frac{R_\Omega}{\sqrt{4ej_0}}, \tag{10}$$

where j_0 is the dark-current density. As follows from Eq. (10), the shape of the spectral characteristic of the detectivity repeats that for the responsivity ($D_\Omega^* \propto R_\Omega$). Since D_Ω^* depends also on the dark-current density $D_\Omega^* \propto 1/\sqrt{j_0}$, it is sensitive to the parameters determining the tunneling of equilibrium carriers from the GNR into the BL, first of all, to the energy states near the Fermi energy ε_{GNR}^F. Considering that the probability of the hole tunneling escape from their Fermi energy can be presented as [compare with Eq. (6)]

$$\Theta_0 \propto \exp\left(-\eta_0^{3/2} \frac{E_{\text{tunn}}}{E_{\text{GNR}}}\right), \tag{11}$$

where $\eta_0 = 1 \pm \varepsilon_{GNR}^F/\Delta_V$ (the sign "+" corresponds the situation when the Fermi level is in the conduction band, so that the GNR array is charged predominately by electrons, and the sign "−" corresponds the situation when the Fermi level is in the GNR valence band), in the most interesting case ($\Sigma > 0$, i.e., the GNR Fermi level is in the conduction band) for the dark-current density we obtain

$$j_0 \simeq \frac{e\Sigma}{\tau_{\text{esc}}} \left(\frac{d}{D}\right) \exp\left[-\left(1 + \frac{\varepsilon_{\text{GNR}}^F}{\Delta_V}\right)^{3/2} \frac{E_{\text{tunn}}}{E_{\text{GNR}}}\right]. \tag{12}$$

Hence,

$$D_\Omega^* = \overline{D}_\Omega^* \frac{2}{\pi} \left(\frac{\Delta}{\hbar\Omega}\right) \sum_{n=1}^{\infty} \mathcal{F}_n \left(\frac{\hbar\Omega}{\Delta}\right), \tag{13}$$

where

$$\overline{D}_\Omega^* = \frac{\overline{R}_\Omega}{\sqrt{4ej_0}} = \frac{\beta}{\hbar\Omega} \frac{\Theta_\Omega}{\sqrt{\Theta_0}} \sqrt{\frac{\tau_{\text{esc}}}{\Sigma}} \propto S_\Omega \exp\left[\left(1 + \frac{\varepsilon_{\text{GNR}}^F}{\Delta_V}\right)^{3/2} \frac{E_{\text{tunn}}}{2E_{\text{GNR}}}\right]. \tag{14}$$

At $\varepsilon_{\text{GNR}}^F > 0$, the exponential factor in Eq. (14), and hence the GNR-IP detectivity can be fairly large. Although, when $\varepsilon_{\text{GNR}}^F$ becomes larger than $\hbar\Omega/2$, S_Ω and $\overline{D}_\Omega^*$ can exhibit a steep drop in line with the pertinent responsivity roll-off seen in Fig. 3(b). This indicated that the selection of the CL and BL parameters, where first of all their doping opens the possibilities of the GNR-IP detectivity enhancement. One needs to stress that the proper choosing of the bias voltage might also be important for the GNR-ID responsivity and detectivity.

4 Detection of Modulated Radiation

If the incident radiation comprises the steady-state and modulation components, I_Ω and $\delta I_\Omega^\omega \exp(-i\omega t)$, respectively, where δI_Ω^ω and ω are the amplitude and frequency of the modulation components, considering the Shockley–Ramo theorem,[38,39] the ac terminal current density is given by [see Eqs. (29) and (30) in the Appendix]

$$\langle \delta j_\Omega^\omega \rangle = e\beta_\Omega \Theta_\Omega^\omega \frac{[\exp(i\omega\tau_{\text{tr}}) - 1]}{i\omega\tau_{\text{tr}}} \delta I_\Omega^\omega, \tag{15}$$

where

$$\Theta_\Omega^\omega \simeq \frac{1}{1 - i\omega\tau_{\text{esc}} + \frac{\tau_{\text{esc}}}{\tau_{\text{relax}}} \exp\left(\eta_\Omega^{3/2} \frac{E_{\text{tunn}}}{E_{\text{GNR}}}\right)}, \tag{16}$$

which replaces Θ_Ω in Eq. (26) and τ_{tr} is the hole transit time across the BL. The factor $[\exp(i\omega\tau_{\text{tr}}) - 1]/i\omega\tau_{\text{tr}}$ in the right-hand side of Eq. (8) describes the hole transit-time effect (transit delay) in the BL.

As follows from Eqs. (8), (15), and (16), for the responsivity to the modulation signals, $R_\Omega^\omega = \langle \delta j_\Omega^\omega \rangle / \hbar\Omega \delta I_\Omega^\omega$ one can arrive at

$$R_\Omega^\omega = R_\Omega \frac{\Theta_\Omega^\omega T^\omega}{\Theta_\Omega}, \tag{17}$$

where

$$T^\omega = \frac{\exp(i\omega\tau_{\text{tr}}) - 1}{i\omega\tau_{\text{tr}}} \tag{18}$$

is the transit-time factor. Hence,

$$\left|\frac{R_\Omega^\omega}{R_\Omega}\right| = \frac{1 + \frac{\tau_{\text{esc}}}{\tau_{\text{relax}}} \exp\left(\eta_\Omega^{3/2} \frac{E_{\text{tunn}}}{E_{\text{GNR}}}\right)}{\sqrt{\left[1 + \frac{\tau_{\text{esc}}}{\tau_{\text{relax}}} \exp\left(\eta_\Omega^{3/2} \frac{E_{\text{tunn}}}{E_{\text{GNR}}}\right)\right]^2 + \omega^2 \tau_{\text{esc}}^2}} \left|\frac{\sin(\omega\tau_{\text{tr}}/2)}{(\omega\tau_{\text{tr}}/2)}\right|. \tag{19}$$

According to Eq. (19), the roll-off of the relative responsivity $|R^\omega_\Omega/R_\Omega|$ with increasing modulation frequency ω is primarily determined by the transit time τ_{tr} if the try-to-escape time τ_{esc} is shorter than the transit time of the holes τ_r

$$\left| \frac{R^\omega_\Omega}{R_\Omega} \right| \simeq \left| \frac{\sin(\omega\tau_{tr}/2)}{(\omega\tau_{tr}/2)} \right|. \tag{20}$$

5 Plasmonic Response

Depending on the sign of $\Sigma = \Sigma_d - \Sigma_a - \kappa_{BL}V/4\pi eW$, the one-dimensional electron or hole gases are formed in each GNR. The collective response of these electron or hole systems can lead to pronounced plasmonic phenomena.

The ac current of the photoexcited holes emitted from the GLs causes ac hole injection from the side contacts to the GNRs. The ac current along the GNRs (in the y direction, see Fig. 1) could lead to the excitation of the plasmonic oscillations, i.e., the self-consistent spatial–temporal variation of the electron or hole density and the GNR array potential in the GNR array $\delta\varphi^\omega_\Omega(y)\exp(-i\omega t)$.[33,40–42] This plasmonic oscillation is the standing wave formed by the plasmonic waves propagated along the GNR in the opposite directions (i.e., with the wave numbers $\pm k_y$). As a result, accounting for the plasmonic oscillations in the GNR, the averaged current density can be presented as [see the Appendix, Eq. (37)]

$$\langle \delta j^\omega_\Omega \rangle = e\beta_\Omega\Theta^\omega_\Omega T^\omega \frac{\tan\left[\pi\sqrt{(\omega+i/\tau)(\omega+i/\tau_d)}/\omega_p\right]}{\left[\pi\sqrt{(\omega+i/\tau)(\omega+i/\tau_d)}/\omega_p\right]}\delta I^\omega_\Omega. \tag{21}$$

Here, $1/\tau_d \propto \beta_\Omega I_\Omega$ is given by Eq. (34) in the Appendix. Equation (21) yields the following equation for the responsivity:

$$R^\omega_\Omega = R_\Omega \frac{\Theta^\omega_\Omega T^\omega P^\omega}{\Theta_\Omega}. \tag{22}$$

Here,

$$P^\omega = \frac{\tan\left[\pi\sqrt{(\omega+i/\tau)(\omega+i/\tau_d)}/2\omega_p\right]}{\left[\pi\sqrt{(\omega+i/\tau)(\omega+i/\tau_d)}/2\omega_p\right]} \tag{23}$$

is the factor describing the contribution of the plasmonic resonances [compare Eqs. (17) and (22)] and $\omega_p = \pi\sqrt{\pi e^2 W\Sigma/\kappa_{BL}mL^2}$ is the plasmonic frequency of the carriers (holes) induced in the GNRs, where $\Sigma \simeq \Sigma_a - \Sigma_d + \kappa_{BL}V/4\pi eW$ is the hole density in the GNR array induced by the doping of the CL and BL and the bias voltage, and $m \simeq \Delta/2v^2_W$ is the hole effective mass in GNRs. Considering the relation between m and Δ, we find

$$\omega_p = \frac{\pi v_W}{L}\sqrt{\frac{2\pi e^2 W\Sigma_a}{\kappa_{BL}\Delta} + \frac{eV}{2\Delta}} = \frac{\pi v_W}{L}\sqrt{\frac{WE_a + eV}{2\Delta}} = \frac{\pi v_W}{L}\sqrt{\frac{WE_{GNR}}{2\Delta}}. \tag{24}$$

Setting $E_{GNR} = 10^6$ V/cm, $\Delta = 100$ meV, $W = 0.1$ μm, and $L = 2.5$ μm, we obtain $\omega_p/2\pi \simeq 1.4$ THz.

If $\omega \ll \tau^{-1}$, $\tau^{-1}_d \ll \omega_p$, one obtains $P^\omega \simeq 1$, and Eq. (22) turns to Eq. (17). At the combined resonance $\hbar\Omega/\Delta \simeq 1$ and $\omega/\omega_p \simeq 1$, the responsivity $|R^\omega_\Omega|$ exhibits a particularly high maximum.

Figure 4 shows examples of the modulation characteristics $|R^\omega_\Omega/R_\Omega|$ as functions of the modulation frequency $\omega/2\pi$. These characteristics account for the delay in the photoexcited holes escape from the GNRs, the hole transit-time delay, and the plasmonic effects.
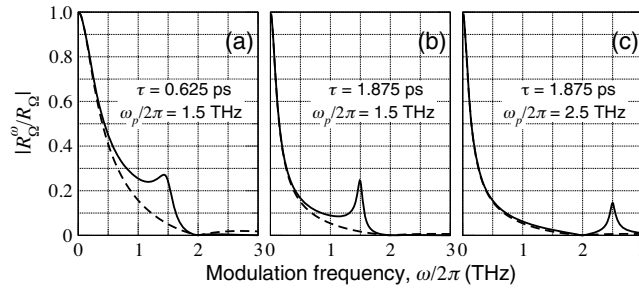
Fig. 4 The responsivity $|R_\Omega^\omega|$ normalized by $|R_\Omega|$ versus the modulation frequency $\omega/2\pi$ for (a) $\omega_p/2\pi = 1.5$ THz and $\tau = 0.625$ ps, (b) $\omega_p/2\pi = 1.5$ THz and $\tau = 1.875$ ps, and (c) $\omega_p/2\pi = 2.5$ THz and $\tau = 1.875$ ps. Dashed lines correspond to the modulation without the excitation of plasmonic oscillation.

The following parameters are assumed: $\omega_p/2\pi = 1.5$ and $\omega_p/2\pi = 2.5$ THz, $\tau_{tr} = 0.5$ ps, $\tau_d = 10$ ps, $\tau_{esc} = \tau = 0.625$ ps and $\tau_{esc} = \tau = 1.875$ ps (corresponding to $\Gamma = \hbar/\tau = 1$ meV and $\Gamma = 1/3$ meV, respectively). The frequency dependences shown in Fig. 4 reflect the interplay of the transit-time and plasmonic effects.

As seen from Fig. 4, $|R_\Omega^\omega/R_\Omega|$ and hence $|R_\Omega^\omega|$ exhibit the maxima corresponding to the plasmonic resonance ω/ω_p. The responsivity $|R_\Omega^\omega|$ becomes particularly large at the combined resonances $\Omega \simeq n\Delta/\hbar$ and $\omega/\omega_p \simeq 1$. The resonance effects under consideration are pronounced when the carrier momentum relaxation time τ is sufficiently long.

The inclusion of the plasmonic effects enables the possibility of the GNR-IPs operation in the terahertz range of the modulation frequencies, in particular, as the terahertz photomixers.

6 Discussion

Both the realization of the resonant interband intersubband radiative transitions and the possibility of the pronounced plasmonic oscillations require relatively perfect GNRs with high carrier mobilities along the GNRs or their ballistic transport, which are achievable in real GNR-based heterostructures. The electron and hole mobilities on the order of $(2000 \text{ to } 2500)$ cm^2/Vs measured in GNRs[43,44] are sufficiently large to support resonant interband transitions and plasmonic oscillations.

As seen from Figs. 3(a) and 3(b), the comparison of the vertical GNR-IP and GL-IP responsivities' dotted lines in [Figs. 3(a) and 3(b)], R_Ω and R_Ω, at $\hbar\Omega = \Delta$ yields $R_\Omega/R_\Omega \gg 1$. The same is valid for $R_\Omega^\omega/R_\Omega^\omega$. Thus, the GNR-IPs can markedly surpass the GL-IPs in the responsivity if the GNRs are sufficiently perfect with long electron and hole momentum relaxation times, in particular, $\tau = (1.25 \text{ to } 6.25) \times 10^{-13}$ s [corresponding to $\Gamma = (1 \text{ to } 5)$ meV], assumed in Figs. 3(a) and 3(b).

Despite a similarity of the GNR-IP and the standard unitraveling-carrier photodiodes, there are the following distinctions enabling the advantages of the former due to the following: the operation in the far-infrared range because of a narrow energy gap in the GNRs and the BLs, an increase photoexcitation efficiency associated with the resonant intersubband transitions, and a shortened escape time of the photoexcited holes.

Comparing the responsivity R_Ω^ω of the vertical GNR-IP under consideration with the responsivity $\overline{R}_\Omega^\omega$ of the lateral GNR-IP with the p–i–n structure having the depleted GNR array (like those considered in Refs. 8 and 45–47) and exploiting the variation of the GNR conductivity under irradiation (with the same lateral sizes), at low- and high-modulation frequencies ω one can find, respectively, $R_\Omega/\overline{R}_\Omega \simeq 2$ and $R_\Omega^\omega \overline{R}_\Omega^\omega \simeq 2\overline{\tau}_{tr}/\tau_{tr}$. Here, $\overline{\tau}_{tr}/\tau_{tr} \simeq (L/W) \gg 1$ is the ratio of the lateral (along the GNRs) and vertical (across the BL) transit times. The responsivity of the lateral GNR-IPs with the n-contacts and the energy barrier formed by the GNR between these contacts[6,8,33] can include the photoconductive gain increasing their responsivity, but at the expense of a lower speed operation.

The structure of the GNR-IP can be inverted placing the BL on the device top. Such GNR-IPs can be made on the hBN substrate.

Due to the similarity of the band alignment of the GNR with the bP and bAs layers, the obtained results can be applied to the GNR-IPs with the b-As layers considering the pertinent quantitative difference in Δ_C and Δ_V.

The resonant response of the GNR-IPs is revealed when the smearing of the carrier spectra is relatively small. This requires a smallness of γ (i.e., sufficiently long momentum relaxation time τ) and a small overlap of the wave functions in the neighboring GNRs. The latter implies that the spacing between these GNRs $l = (D - d)$ should not be too small. This condition looks like $\exp[-2\sqrt{2m_z(\Delta_V - \Delta/2)}(D - d)/\hbar] \ll 1$. For the GNR-IPs operating at the photon energies $\hbar\Omega \sim 100$ meV, $d \sim 4$ nm, the above inequality is satisfied if $D - d > 0.4$ nm. This means that the spacing between the GNRs can be fairly small, so that $d/D \leq 1$ and the potential sag in the inter-GNR region is small. All these indicate that the lateral nonuniformity of the potential in the GNR array plane can be very small.

7 Conclusions

We proposed and evaluated interband far-infrared photodetectors with the GNR array and the bP BL—GNR-IPs. Due to the specifics of the energy spectra of graphene and bP, the GNR-IPs can operate at photon energies much smaller than 300 meV. Due to a strong interband resonant absorption in the GNRs, the GNR-IPs can surpass the interband GL-IPs and different inter-sub-band IPs in responsivity and detectivity. The GNR-IPs are analogous to the unitraveling-carrier photodiodes and can operate at fairly high-modulation frequencies of the incident radiation. The possibility of the excitation of plasmonic oscillations in the GNR array of the device might lead to a pronounced response when the radiation modulation frequency is close to the frequency of the plasmonic oscillations, which is typically in the terahertz range. This enables the use of the GNR-IPs as terahertz photomixers. The GNR-IP response can be particularly strong at the combined resonance—the radiation frequency corresponds to the resonant interband transitions between the sub-bands, whereas the radiation modulation frequency corresponds to the plasmonic resonance.

8 Appendix

8.1 Steady-State Photocurrent

Considering that the incident radiation comprises the steady-state and modulation components, I_Ω and $\delta I_\Omega^\omega \exp(-i\omega t)$, respectively, where δI_Ω^ω and ω are the amplitude and frequency of the modulation component, the dc and ac components of surface density, Σ_Ω and $\delta\Sigma_\Omega^\omega$, of the photo-excited carriers in the GNR array averaged in the lateral directions $\Sigma_\Omega + \delta\Sigma_\Omega^\omega$ is governed by the following equations:

$$\beta_\Omega I_\Omega - \Sigma_\Omega \left[\frac{1}{\tau_{\text{relax}}} + \frac{\exp(-\eta_\Omega^{3/2} E_{\text{tunn}}/E_{\text{GNR}})}{\tau_{\text{esc}}}\right] = \frac{d\Sigma_\Omega}{dt} = 0, \tag{25}$$

$$\beta_\Omega \delta I_\Omega^\omega - \delta\Sigma_\Omega^\omega \left[\frac{1}{\tau_{\text{relax}}} + \frac{\exp(-\eta_\Omega^{3/2} E_{\text{tunn}}/E_{\text{GNR}})}{\tau_{\text{esc}}}\right] = \frac{\delta\Sigma_\Omega^\omega}{dt}. \tag{26}$$

The parameters in Eqs. (25) and (26) were given in the main text.

The dc components of the average current density are given by

$$\langle j_\Omega \rangle = \frac{e \exp(-\eta_\Omega^{3/2} E_{\text{tunn}}/E_{\text{GNR}})}{\tau_{\text{esc}}} \Sigma_\Omega. \tag{27}$$

Equations (25) and (27) yield Eq. (2) with the factors determined by Eqs. (3)–(6).

8.2 *Photocurrent at Modulated Radiation*

The ac component of the average terminal current density is equal to

$$\langle\delta j_\Omega^\omega\rangle = \frac{e \, \exp(-\eta_\Omega^{3/2} E_{\text{tunn}}/E_{\text{GNR}})}{\tau_{\text{esc}}} \frac{[\exp(i\omega\tau_{\text{tr}}) - 1]}{i\omega\tau_{\text{tr}}} \delta\Sigma_\Omega^\omega. \tag{28}$$

Here, τ_{tr} is the transit time of the carriers crossing the BL. This time can be estimated as $\tau_{\text{tr}} = W/v_S$, where v_S is the average (or saturation) velocity in the BL. The factor containing τ_{tr} describes the effect of transit-time finiteness on the induced terminal current in line with the Shockley–Ramo theorem.[38,39] Equation (28) does not account for the possible excitation of plasma oscillations (spatiotemporal variations of the carrier density in the GNR-array and of the electric field in the BL), which could result in the temporal variation of E_{GNR} and in the displacement terminal current. Such a simplification of Eq. (28) is justified when ω is far from the characteristic plasma frequencies.

Equations (26) and (28) yield

$$\langle\delta j_\Omega^\omega\rangle = \frac{e\beta_\Omega}{1 - i\omega\tau_{\text{esc}} + \frac{\tau_{\text{esc}}}{\tau_{\text{relax}}} \exp\left(\eta_\Omega^{3/2} \frac{E_{\text{tunn}}}{E_{\text{GNR}}}\right)} \frac{[\exp(i\omega\tau_{\text{tr}}) - 1]}{i\omega\tau_{\text{tr}}} \delta I_\Omega^\omega \quad = e\beta_\Omega\Theta_\Omega^\omega T^\omega\delta I_\Omega^\omega, \tag{29}$$

where

$$\Theta_\omega^\omega \simeq \frac{1}{1 - i\omega\tau_{\text{esc}} + \frac{\tau_{\text{esc}}}{\tau_{\text{relax}}} \exp\left(\eta_\Omega^{3/2} \frac{E_{\text{tunn}}}{E_{\text{GNR}}}\right)}, \quad T^\omega = \frac{\exp(i\omega\tau_{\text{tr}}) - 1}{i\omega\tau_{\text{tr}}}. \tag{30}$$

8.3 *Plasmonic Oscillations in GNR Arrays*

The amplitude of the plasmonic mode potential $\delta\varphi_\Omega^\omega$ is governed by the equation, which is the consequence of the electron transport equation along the GNR and the Poisson equation (similar to that used previously for different plasmonic structures)[33,40,41]

$$\frac{d^2\delta\varphi_\Omega^\omega}{dy^2} + \frac{\omega(\omega + i/\tau)}{s^2}\delta\varphi_\Omega^\omega = i(\omega + i/\tau)\frac{4\pi W}{\kappa_{\text{BL}}s^2}\delta j_\Omega^\omega, \tag{31}$$

with the boundary conditions $\delta\varphi_\Omega^\omega|_{y=0} = 0$ (at the contact) and $d\delta\varphi_\Omega^\omega/dy|_{y=L} = 0$ (at free GNR ends). Here, $s = \sqrt{4\pi e^2 W\Sigma/\kappa_{\text{BL}}m}$ is the characteristic plasma velocity in the GNR array separated from the highly conducting p$^+$ substrate by the BL of the thickness W,[7] Σ is the hole density in the GNR array, m is the effective mass in the GNRs, and L is the length of the GNRs (spacing between the side contacts to the GNRs).

Since the ac current δj_Ω^ω apart from the current due to the variation of the radiation intensity includes the component arisen due to the variations of the tunneling probability associated with the change of the electric field at the GNR array δE_{GNR} in the case of the plasmonic oscillations, Eq. (29) should be replaced by

$$\delta j_\Omega^\omega = e\beta_\Omega T^\omega\left[\Theta_\Omega^\omega\delta I_\Omega^\omega - \frac{I_\Omega}{W}\left(\frac{d\Theta_\Omega^\omega}{dE_{\text{GNR}}}\right)\delta\varphi_\Omega^\omega\right] = e\beta_\Omega T^\omega\Theta_\Omega^\omega\delta I_\Omega^\omega - \frac{\kappa_{\text{BL}}}{4\pi W\tau_d}\delta\varphi_\Omega^\omega, \tag{32}$$

so that Eq. (31) becomes

$$\frac{d^2\delta\varphi_\Omega^\omega}{dy^2} + \frac{(\omega + i/\tau)(\omega + i/\tau_d)}{s^2}\delta\varphi_\Omega^\omega = i(\omega + i/\tau)\frac{4\pi W}{\kappa_{\text{BL}}s^2}e\beta_\Omega\Theta_\Omega^\omega T^\omega\delta I_\Omega^\omega, \tag{33}$$

where

$$\frac{1}{\tau_d} = \frac{4\pi e\beta_\Omega I_\Omega}{\kappa_{\text{BL}}}\left(\frac{d\Theta_\Omega^\omega}{dE_{\text{GNR}}}\right)T^\omega. \tag{34}$$

Solving Eq. (33) with the above boundary conditions, we obtain

$$\varphi_{\Omega}^{\omega} = \frac{i4\pi W}{\kappa_{\mathrm{BL}}} \frac{e\beta_{\Omega}\Theta_{\Omega}^{\omega}T^{\omega}}{(\omega + i/\tau_d)} \left\{ 1 - \frac{\cos\left[\sqrt{(\omega + i/\tau)(\omega + i/\tau_d)}(L - y)/s\right]}{\cos\left[\sqrt{(\omega + i/\tau)(\omega + i/\tau_d)}L/s\right]} \right\} \delta I_{\Omega}^{\omega}, \qquad (35)$$

so that

$$\langle \varphi_{\Omega}^{\omega} \rangle = \frac{i4\pi W}{\kappa_{\mathrm{BL}}} \frac{e\beta_{\Omega}\Theta_{\Omega}^{\omega}T^{\omega}}{(\omega + i/\tau_d)} \left\{ 1 - \frac{\tan\left[\pi\sqrt{(\omega + i/\tau)(\omega + i/\tau_d)}/2\omega_p\right]}{\left[\pi\sqrt{(\omega + i/\tau)(\omega + i/\tau_d)}/2\omega_p\right]} \right\} \delta I_{\Omega}^{\omega}, \qquad (36)$$

where $\omega_p = \pi s/2L = \pi\sqrt{\pi e^2 W\Sigma/\kappa_{\mathrm{BL}}mL^2}$ is the plasmonic frequency.

Adding the density of the displacement current $\delta i_{\Omega}^{\omega} = i\omega(\kappa_{\mathrm{BL}}/4\pi W)\delta\varphi_{\Omega}^{\omega}$ to $\delta j_{\Omega}^{\omega}$, we find

$$\langle \delta j_{\Omega}^{\omega} \rangle = e\beta_{\Omega}\Theta_{\Omega}^{\omega}T^{\omega}\delta I_{\Omega}^{\omega} + i\frac{\kappa_{\mathrm{BL}}}{4\pi W}\left(\omega + \frac{i}{\tau_d}\right)\langle\delta\varphi_{\Omega}^{\omega}\rangle$$

$$= e\beta_{\Omega}\Theta_{\Omega}^{\omega}T^{\omega}\frac{\tan\left[\pi\sqrt{(\omega + i/\tau)(\omega + i/\tau_d)}/\omega_p\right]}{\left[\pi\sqrt{(\omega + i/\tau)(\omega + i/\tau_d)}/\omega_p\right]}\delta I_{\Omega}^{\omega}. \qquad (37)$$

8.4 *Fermi Energy in the GNR Array*

If $\Sigma = \Sigma_d - \Sigma_a - \kappa_{\mathrm{BL}}V/4\pi eW > 0$, i.e., at a stronger doping of the CL than the BL and at not too high bias voltages, the GNRs are occupied primarily by the induced electrons. At sufficiently large Σ, the electron gas in the GNRs can be degenerate. In this case, the linear electron density in GNRs is given by

$$\rho \simeq \frac{1}{\pi\hbar}\int_{-p^F}^{p^F} \mathrm{d}p = \frac{2p^F}{\pi\hbar}. \qquad (38)$$

Here, p^F is the electron momentum at the Fermi energy. The average surface electron density is equal $\Sigma = \rho/D$, so that

$$\Sigma \simeq \frac{2p^F}{\pi\hbar D}. \qquad (39)$$

At not too high electron densities when the electrons occupy only the lowest sub-band $n = 1$, considering Eq. (1), we have

$$\varepsilon_{\mathrm{GNR}}^F \simeq \Delta\left(\frac{p^F d}{2\pi\hbar}\right)^2. \qquad (40)$$

Hence,

$$\varepsilon_{\mathrm{GNR}}^F \simeq \Delta\left(\frac{\Sigma dD}{4}\right)^2 \leq \Delta\left(\frac{\Sigma d^2}{4}\right)^2. \qquad (41)$$

Acknowledgments

References

1. C. Berger et al., "Electronic confinement and coherence in patterned epitaxial graphene," *Science* **312**, 1191 (2006).
2. Y.-W. Son, M. L. Cohen, and S. G. Louie, "Half-metallic graphene nanoribbons," *Nature* **444**, 347 (2006).
3. M. Y. Han et al., "Energy band-gap engineering of graphene nanoribbons," *Phys. Rev. Lett.* **98**, 206805 (2007).
4. L. Yang et al., "Quasiparticle energies and band gaps in graphene nanoribbons," *Phys. Rev. Lett.* **99**, 186801 (2007).
5. L. Brey and H. A. Fertig, "Elementary electronic excitations in graphene nanoribbons," *Phys. Rev. B* **75**, 125434 (2007).
6. V. Ryzhii et al., "Device model for graphene nanoribbon phototransistor," *Appl. Phys. Express* **1**, 063002 (2008).
7. V. V. Popov et al., "Oblique terahertz plasmons in graphene nanoribbon arrays," *Phys. Rev. B* **81**, 073404 (2010).
8. V. Ryzhii et al., "Terahertz and infrared photodetectors based on multiple graphene layer and nanoribbon structures," *Opto-Electron. Rev.* **20**, 15–20 (2012).
9. R. W. Keyes, "The electrical properties of black phosphorous," *Phys. Rev.* **92**, 580 (1953).
10. A. Morita, "Semiconducting black phosphorus," *Appl. Phys. A* **39**, 227 (1986).
11. H. Asahina and A. Morita, "Band structure and optical properties of black phosphorus," *J. Phys. C* **17**, 1839 (1984).
12. X. Ling et al., "The renaissance of black phosphorus," *Proc. Natl. Acad. Sci. U. S. A.* **112**, 4523 (2015).
13. H. Liu et al., "Phosphorene: an unexplored 2D semiconductor with a high hole mobility," *ACS Nano* **8**, 4033 (2014).
14. Y. Xu, J. Dai, and X. C. Zeng, "Electron-transport properties of few-layer black phosphorous," *J. Phys. Chem. Lett.* **6**, 1996 (2015).
15. F. Xia, H. Wang, and Y. Jia, "Rediscovering black phosphorous as an anisotropic layered material for optoelectronics and electronics," *Nat. Commun.* **5**, 4458 (2014).
16. M. Engel, M. Steiner, and P. Avouris, "A black phosphorus photo-detector for multispectral high-resolution imaging," *Nano Lett.* **14**, 6414 (2014).
17. A. Castellanos-Gomez, "Black phosphorus: narrow gap, wide applications," *J. Phys. Chem. Lett.* **6**, 4280 (2015).
18. M. Batmunkh, M. Bat-Erdene, and J. G. Shapter, "Phosphorene and phosphorene-based materials—prospects for future applications," *Adv. Mater.* **28**, 8586 (2016).
19. J. Qiao et al., "High-mobility transport anisotropy and linear dichroism in few-layer black phosphorus," *Nat. Commun.* **5**, 4475 (2014).
20. V. Ryzhii et al., "Electrical modulation of terahertz radiation using graphene-phosphorene heterostructures," *Semicond. Sci. Technol.* **33**, 124010 (2018).
21. V. Ryzhii et al., "Negative terahertz conductivity at vertical carrier injection in a black-arsenic-phosphorus-graphene heterostructure integrated with a light-emitting diode," *IEEE J. Sel. Top. Quantum Electron.* **25**, 2000209 (2019).
22. V. Ryzhii et al., "Negative terahertz conductivity and amplification of surface plasmons in graphene-black phosphorus injection laser heterostructures," *Phys. Rev. B* **100**, 115436 (2019).
23. V. Ryzhii et al., "Real-space-transfer mechanism of negative differential conductivity in gated graphene-phosphorene hybrid structures: phenomenological heating model," *J. Appl. Phys.* **124**, 114501 (2018).
24. V. Ryzhii et al., "Negative photoconductivity and hot-carrier bolometric detection of terahertz radiation in graphene-phosphorene hybrid structures," *J. Appl. Phys.* **125**, 151608 (2019).

25. M. Y. Morozov et al., "Optical pumping in graphene-based terahertz/far-infrared super-luminescent and laser heterostructures with graded-gap black-$P_x As_{1−x}$ absorbing-cooling layers," *Opt. Eng.* **59**, 061606 (2019).
26. V. Ryzhii et al., "Far-infrared photodetectors based on graphene/black-AsP heterostructures," *Opt. Express* **28**, 2480–2498 (2020).
27. Y. Cai, C. Zhang, and Y.-W. Zhang, "Layer-dependent band alignment and work function of few-layer phosphorene," *Sci. Rep.* **4**, 6677 (2014).
28. B. Liu et al., "Black arsenic–phosphorus: layered anisotropic infrared semiconductors with highly tunable compositions and properties," *Adv. Mater.* **27**, 4423–4429 (2015).
29. M. Long et al., "Room temperature high-detectivity mid-infrared photodetectors based on black arsenic phosphorus," *Sci. Adv.* **3**(6), e1700589 (2017).
30. S. Yuan et al., "Air-stable room-temperature mid-infrared photodetectors based on hBN/black arsenic phosphorus/hBN heterostructures," *Nano Lett.* **18**, 3172–3179 (2018).
31. L. Yu et al., "Electrically tunable optical properties of few-layer black arsenic phosphorus," *Nanotechnology* **29**, 484001 (2018).
32. Y. Chen et al., "Black arsenic: a layered semiconductor with extreme in-plane anisotropy," *Adv. Mater.* **30**, 1800754 (2018).
33. V. Ryzhii et al., "Graphene nanoribbon phototransistor: proposal and analysis," *Jpn. J. Appl. Phys.* **48**, 04C144 (2009).
34. T. Ishibashi and H. Ito, "Uni-traveling-carrier photodiodes," Tech. Dig. Ultrafast Electronics and Optoelectronics, Lake Tahoe, California, pp. 83–87 (1997).
35. H. Ito et al., "Photonic generation of continuous THz wave using uni-traveling-carrier photodiode," *J. Lightwave Technol.* **23**, 4016–4021 (2005).
36. A. Wakatsuki, Y. Muramoto, and T. Ishibashi, "Development of terahertz-wave photo-mixer module using a uni-traveling-carrier photodiode," NTT Technical Review 10, No. 2 (2012).
37. S. Luryi, "Quantum capacitance devices," *Appl. Phys. Lett.* **52**, 501–503 (1988).
38. W. Shockley, "Currents to conductors induced by a moving point charge," *J. Appl. Phys.* **9**, 635 (1938).
39. S. Ramo, "Currents induced by electron motion," *Proc. IRE* **27**, 584–585 (1939).
40. V. Ryzhii and M. Shur, "Tunneling- and barrier-injection transit-time mechanisms of terahertz plasma instability in high-electron mobility transistors," *Semicond. Sci. Technol.* **17**, 1168–1171 (2002).
41. V. Ryzhii et al., "Plasma mechanism of terahertz photomixing in high-electron mobility transistor under interband photoexcitation," *J. Appl. Phys.* **92**, 5756–5760 (2002).
42. M. Ryzhii, V. Ryzhii, and M. S. Shur, "Effect of near-ballistic photoelectron transport on resonant plasma-assisted photomixing in high-electron mobility btransistors," *Semicond. Sci. Technol.* **19**, S74–S76 (2004).
43. Y. Li et al., "Graphene plasmonic devices for terahertz optoelectronics," *Nanophotonics* **9**, 1901–1920 (2020).
44. K. Bang et al., "Effect of ribbon width on electrical transport properties of graphene nanoribbons," *Nano Convergence* **5**, 7 (2018).
45. V. Ryzhii et al., "Terahertz and infrared photodetection using p-i-n multiple-graphene-layer structures," *J. Appl. Phys.* **107**, 054512 (2010).
46. E. Ahmadi, A. Asgari, and K. Ahmadiniar, "The optical responsivity in IR-photodetector based on armchair graphene nanoribbons with p–i–n structure," *Superlattices Microstruct.* **52**, 605–611 (2012).
47. E. Ahmadi and A. Asgari, "Modeling of the infrared photodetector based on multi layer armchair graphene nanoribbons," *J. Appl. Phys.* **113**, 093106 (2013).

Maxim Ryzhii is currently a senior associate professor at the University of Aizu, Aizu-Wakamatsu, Japan. His research activity includes physics and computer modeling of optoelectronic and terahertz nanostructure devices, and computational modeling of biophysical systems. He is the author or coauthor of more than 180 journal publications and numerous conference papers. He is a senior member of the IEEE and a member of the APS.

Victor Ryzhii is currently a principle researcher at the Institute of Ultra-High Frequency Semiconductor Electronics and a visiting professor at the Research Institute of Electrical Communication, Tohoku University, Japan. He is the author and coauthor of more than 400 research publications in the theory and computer modeling of micro- and nanostructures and electronic and optoelectronic devices and holds 11 patents. He is a corresponding member of the RAS and a fellow of the IEEE and the APS.

Petr P. Maltsev is currently a scientific director at the Institute of Ultra-High Frequency Semiconductor Electronics of RAS, Moscow, Russia. He graduated from Tashkent University of Information Technologies in 1971. Since 1998, he has been a professor at Moscow State Institute of Radio Engineering, Electronics, and Automation. He has more than 250 papers in refereed journals, 40 patents, and 7 monographs.

Dmitry S. Ponomarev works as a deputy director at the Institute of Ultra-High Frequency Semiconductor Electronics of RAS, Moscow, Russia. He is also a leading researcher at A. M. Prokhorov General Physics Institute of RAS and Moscow Institute of Physics and Technology, Moscow, Russia. His research interests are focused on photonic devices, terahertz spectroscopy, and plasmonics.

Vladimir G. Leiman is currently a professor in the Department of General Physics and a principle researcher at the 2-D Material's Optoelectronics Laboratory, Moscow Institute of Physics and Technology, Russia. His research interests include the theory of intensive electron beams in vacuum and plasma devices and plasmonic phenomena in electronic and optoelectronic devices. He is the author and coauthor of more than 100 journal publications and numerous conference papers. He is a member of the OSA.

Valery E. Karasik is a professor in the Department of Radioelectronics and a director at the Center of Photonics and Infrared Engineering of Bauman Moscow State Technical University. His interests include the research and design of laser devices with the focus on the laser target detection and location. He is a member of the Russian Academy of EII.

Vladimir Mitin is currently SUNY distinguished professor in the Department of Electrical Engineering at the University at Buffalo, the State University of New York. His fields of specialization are microelectronic, nanoelectronic, and optoelectronic devices and materials with special emphasis on sensors and detectors based on nanostructures. He has more than 300 publications including 10 patents, 4 monographs, and 6 textbooks. He is a fellow of the IEEE, the APS, and other professional societies.

Michael S. Shur is the Roberts professor in the Department of Electrical, Computer, and Systems Engineering, Rensselaer Polytechnic Institute, Troy, New York, USA. He is a cofounder of Electronics of the Future, Inc. He is a fellow the IEEE, APS, Electrochemical Society, and a foreign member of the Lithuanian Academy of Sciences and several other professional societies.

Taiichi Otsuji is a professor at the Research Institute of Electrical Communication, Tohoku University, Sendai, Japan. His current research interests include terahertz electronic and photonic materials/devices and their applications. He has authored and coauthored more than 400 research publications. He is a senior member of the Optical Society of America, a fellow of the IEEE and the APS, and several other professional societies.